Effect of temperature on the formation of Highly-oxygenated Organic Molecules (HOM) from alpha-pinene ozonolysis

Lauriane L. J. QUÉLÉVER [1], Kasper KRISTENSEN [2*], Louise NORMANN JENSEN [2], Bernadette ROSATI [2,3], Ricky TEIWES [2,3], Kaspar R. DAELLENBACH [1], Otso PERÄKYLÄ [1], Pontus ROLDIN [4], Henrik B. PEDERSEN [3], Marianne GLASIUS [2], Merete BILDE [2] and Mikael EHN [1].

[1] Institute for Atmospheric and Earth System Research – INAR / Physics, P.O. Box 64, FI-00014 University of Helsinki, Finland.

[2] Aarhus University, Department of Chemistry, Langelandsgade 140, DK-8000 Aarhus C, Denmark.

[3] Aarhus University, Department of Physics and Astronomy, Ny Munkegade 120, DK-8000 Aarhus C, Denmark.

[4] Lund University, Division of Nuclear Physics, P.O. Box 118, SE-22100 Lund, Sweden.

[*] Presently at University of California, Department of Environmental Science, Policy and Management, Hilgard Hall 251B, CA-94720-3114 Berkeley, United States of America.

Correspondence to Lauriane L.J. QUÉLÉVER (Lauriane.quelever@helsinki.fi) *&* Mikael EHN (Mikael.ehn@helsinki.fi)

Abstract

Highly-oxygenated Organic Molecules (HOM) are important contributors to Secondary Organic Aerosol (SOA) and New-Particle Formation (NPF) in the boreal atmosphere. This newly discovered class of molecules is efficiently formed from atmospheric oxidation of biogenic volatile organic compounds (VOC), such as monoterpenes, through a process called autoxidation. This process, in which peroxy-radical intermediates isomerize to allow addition of molecular oxygen, is expected to be highly temperature-dependent. Here, we

27 studied the dynamics of HOM formation during α-pinene ozonolysis experiments performed at three different

28 temperatures, 20 °C, 0 °C and -15 °C, in the Aarhus University Research on Aerosol (AURA) chamber. We

29 found that the HOM formation, under our experimental conditions (50 ppb α-pinene, 100 ppb ozone),

30 decreased considerably as temperature decreased, with molar yields dropping by around a factor of 50 when

31 experiments were performed at 0 °C, compared to 20 °C. At -15 °C, the HOM signals were already close to

32 the detection limit of the nitrate-based Chemical Ionization Atmospheric Pressure interface Time Of Flight

33 (CI-APi-TOF) mass spectrometer used for measuring gas-phase HOM. Surprisingly, very little difference was

34 seen in the mass spectral distribution of the HOM molecules of interest at 0 °C and 20 °C, with e.g. the ratios

35 between the typical HOM products $C_{10}H_{14}O_7$, $C_{10}H_{14}O_9$, and $C_{10}H_{14}O_{11}$ remaining fairly constant. The more

36 oxidized species have undergone more isomerization steps, yet, at lower temperature, they did not decrease

37 more than the less oxidized species. One possible explanation is be that the rate-limiting step forming these

38 HOM occurs before the products become oxygenated enough to be detected by our CI-APi-TOF (i.e. typically

39 seven or more oxygen atoms). The strong temperature dependence of HOM formation was observed under

40 temperatures highly relevant for the boreal forest, but the exact magnitude of this effect in the atmosphere will

41 be much more complex: the fate of peroxy-radicals is a competition between autoxidation (influenced by

42 temperature and VOC type) and bimolecular termination pathways (influenced mainly by concentration of

43 reaction partners). While the temperature influence is likely smaller in the boreal atmosphere than in our

44 chamber, the magnitude and complexity of this effect clearly deserves more consideration in future studies in

45 order to estimate the ultimate role of HOM on SOA and NPF under different atmospheric conditions.

46

47 **Keywords:** HOM formation & yield, Temperature, ACCHA campaign, AURA chamber, Mass Spectrometry,

48 CI-APi-TOF

49

50 # 1. Introduction

51

52 Aerosol particles impact Earth's climate by scattering and absorbing solar radiation, and by influencing cloud

53 properties when they act as Cloud Condensation Nuclei (CCN) (IPCC, 2013). Organic compounds contribute

54   significantly to the chemical composition of aerosol, accounting from 20 % to 90 % of the total aerosol mass

55   of sub-micrometer particles depending on their location in the globe (Jimenez et al., 2009). Submicron organic

56   aerosol are dominantly secondary. Called Secondary Organic Aerosol (SOA), they originate from gas-to-

57   particle conversion from condensable vapors (Hallquist et al., 2009; Zhang et al., 2007). These vapors are

58   mainly oxidation products of Volatile Organic Compounds (VOC), having sufficiently low vapor pressure (i.e.

59   volatility) to condense onto aerosol particles (Hallquist et al., 2009).

60

61   In order to interact efficiently with solar radiation or to activate cloud droplets, aerosol particles need to be

62   around 100 nm in diameter or larger (Dusek et al., 2006). If particles have formed through nucleation processes

63   in the atmosphere (e.g. Kulmala et al., 2013), their ability to grow to climate-relevant sizes before being

64   scavenged through coagulation is critically impacted by the rate at which low-volatile vapors will condense

65   onto them (Donahue et al., 2013). Extremely Low-Volatile Organic Compounds (ELVOC), introduced by

66   Donahue et al. (2012), have the ability to condense irreversibly onto even the smallest aerosol particles and

67   clusters and thus contribute to particle growth. Low-Volatile Organic Compounds (LVOC), typically more

68   abundant in the atmosphere, are important for the growth of particles larger than a few nanometers (Tröstl et

69   al., 2016).

70

71   Highly-oxygenated Organic Molecules (HOM, Ehn et al., 2014 & 2017) were recently identified as a large

72   contributor to (E)LVOC and the growth of newly formed particles (Ehn et al., 2014; Tröstl et al., 2016). First

73   observed in measurements of naturally charged ions in the boreal forest (Ehn et al., 2010 & 2012) using the

74   Atmospheric Pressure interface Time Of Flight (APi-TOF) mass spectrometer (Junninen et al., 2010), HOM

75   quantification only became possible through the application of nitrate ion chemical ionization (CI) mass

76   spectrometry (Zhao et al., 2013; Ehn et al., 2014). Most studies have utilized the APi-TOF coupled to such a

77   chemical ionization source (CI-APi-TOF, Jokinen et al., 2012), and detailed laboratory studies have been able

78   to elucidate the primary formation pathways of HOM (Rissanen et al., 2014; Jokinen et al., 2014; Mentel et

79   al., 2015). We also note that the HOM-related terminology has evolved over the last years, and here we define

80   HOM as organic molecules formed through gas-phase autoxidation, containing six or more oxygen atoms.

81

82   The main process in HOM formation is peroxy-radical (RO_2) autoxidation (Crounse et al., 2013), which

83   involves an intramolecular H-abstraction by the peroxy-radical group to form a hydroperoxide and a carbon-

84   centered radical to which molecular oxygen (O_2) can rapidly add to form a new RO_2 with a higher level of

85   oxygenation. The efficiency of this process is mainly determined by the availability of easily "abstractable"

86   H-atoms, and such are often formed in the ozonolysis of endocyclic alkenes (Rissanen et al., 2014 & 2015;

87   Berndt et al., 2015). This structural component can be found in many biogenic VOC, such as monoterpenes,

88   enhancing their roles as SOA precursors through efficient autoxidation and HOM formation (Ehn et al., 2014;

89   Jokinen et al., 2014; Berndt et al., 2016). Peroxy-radicals are important intermediates in nearly all atmospheric

90   oxidation processes. The RO_2 that have undergone autoxidation will terminate to closed-shell species in similar

91   ways as less oxidized RO_2, taking place either by unimolecular processes leading to loss of OH or HO_2, or

92   bimolecular reactions with NO, HO_2 or other RO_2. The termination pathway strongly influences the type of

93   HOM that can be formed, with e.g. RO2 + RO2 reactions being able to form ROOR dimers and RO2+NO

94   often forming organic nitrates (Ehn et al., 2014; Berndt et al., 2018). All these bimolecular reactions of peroxy-

95   radicals, as well as the initial oxidant-VOC reaction, are temperature-dependent. For example, the reaction rate

96   of ozone with α-pinene, a broadly studied SOA-forming system, is $6.2 \cdot 10^{17} \, (\pm 1.3 \cdot 10^{17}) \, cm^3 \, molec^{-1} \, s^{-1}$ at 3

97   °C, and $8.3 \cdot 10^{17} \, (\pm 1.3 \cdot 10^{17}) \, cm^3 \, molec^{-1} \, s^{-1}$ at 22 °C (Atkinson et al., 1982). However, the intramolecular

98   isomerization through H-shifts is likely to have a much stronger temperature dependence, due to the higher

99   energy barrier for the H-shift (Seinfeld and Pandis, 2006; Otkjær et al., 2018). As an example (Praske et al.,

100   2018) reported theoretical estimates of different H-shifts in hexane-derived RO_2 which increased roughly by

101   a factor of 5 to10 when the temperature increases by 22 °C (from 23 °C to 45 °C). Possible changes in HOM

102   formation as a function of temperature are thus expected to derive mainly from changes in the autoxidation

103   process. However, a detailed mechanistic understanding the various autoxidation steps, let alone their

104   temperature dependencies, is still lacking for most atmospheric VOC-oxidant systems, owing partly to the

105   plethora and the complexity of the possible reaction pathways.

106

107   Despite recent work in determining the impact of temperature on aerosol formation (Kristensen et al., 2017;

108   Stolzenburg et al., 2018), literature on corresponding HOM effects are extremely limited. At room temperature

109 (i.e. 20 ±5 °C), HOM molar yields have been estimated to be some percent for most monoterpenes in reactions

110 with ozone or OH (Ehn et al., 2014; Jokinen et al., 2015). Only very recently, studies were presented where

111 HOM formation experiments have been conducted at varying temperatures. Stolzenburg et al. (2018) showed

112 that at lower temperatures, the CI-APi-TOF detects much lower HOM concentrations, though no quantitative

113 values on the HOM yields were given. The impact of decreased HOM on new-particle growth rates was

114 compensated by less oxidized species being able to condense at the lower temperatures. In another study, Frege

115 et al. (2018) also concluded that HOM formation decreased at lower temperatures, but their study was based

116 on observations of naturally charged ions using an APi-TOF, complicating the interpretation of HOM

117 formation rates.

118

119 In this study, we directly evaluate the impact of temperature on HOM yields in a laboratory chamber during

120 α-pinene ozonolysis experiments at 20 °C, 0 °C and -15 °C. Relative changes in HOM formation are compared

121 between temperatures both for total HOM yields as well as on a molecule-by-molecule basis. The more

122 detailed impact of temperature on the molecular distribution of HOM is expected to provide new insights into

123 critical steps in the formation pathways.

124

125 2. Methods

126

127 2.1. The AURA Chamber

128 A detailed description of the AURA chamber can be found in Kristensen et al. (2017). Essentially, it consists

129 of a 5 m^3 Teflon® bag contained in a temperature-controlled enclosure. Configured in batch sampling mode,

130 the chamber was initially cleaned by flushing at 20 °C with purified ambient air (i.e. filtered air exempt of

131 particles, water vapor and VOC, and reduced NOx concentration), and subsequently set to the desired

132 temperature and finally filled with the necessary reagents. Over the course of the experiment, it was

133 progressively emptied due to sampling by the measuring instrumentation. In our experiments, we first added

134 ozone to a concentration of 100 ppb, provided by an ozone generator (Model 610, Jelight Company, Inc.) after

135 which the oxidation reaction started when the VOC was introduced by vaporization of a calculated volume of

136   liquid reagent (α-pinene or β-pinene) into a hot stream of nitrogen, reaching the desired VOC concentration

137   (10 or 50 ppb).

138

2.2. The ACCHA Experiment

140   The Aarhus Chamber Campaign on HOM and Aerosols (ACCHA) experiment aimed to explore oxidation

141   processes and aerosol formation during dark monoterpene ozonolysis at different temperatures, from -15 °C

142   to 20 °C. In practice, the experimental plan focused on α-pinene oxidation at two different concentrations (10

143   ppb and 50 ppb) for three different temperatures: -15 °C, 0 °C and 20 °C. Two additional experiments were

144   conducted with temperatures ramped from the coldest to the warmest or reversely during experiments at 10

145   ppb of α-pinene. For comparison, fixed temperature runs were also performed using β-pinene, at a

146   concentration of 50 ppb. Ozone (100 ppb) was used as the main oxidant, but hydroxyl radicals also took part

147   in the oxidation reactions as OH-scavengers were not employed in the experiments discussed here. According

148   to model simulations using the master chemical mechanism v3.3.1 (Jenkin et al., 1997 & 2015; Saunders et

149   al., 2003), ozonolysis accounted for approximately 2/3 and OH-oxidation for 1/3 of the α-pinene oxidation

150   respectively. A table summarizing the experiments of the campaign can be found in the Appendix (Table A1).

151

2.3. Instrumentation

153   The ACCHA experiment involved a diverse set of instruments measuring both the gas phase and the particle

154   phase. The gas phase instrumentation included a Proton Transfer Reaction Time Of Fight Mass Spectrometer

155   (PTR-TOF-MS, Model 8000-783, IONICON Inc., Jordan et al., 2009) for measuring the concentrations of the

156   injected VOCs and other volatile products, as well as a nitrate-based Chemical Ionization Atmospheric

157   Pressure interface Time of Flight (CI-APi-TOF, TOFWERK A.G. & Aerodyne Research Inc., Jokinen et al.,

158   2012) mass spectrometer, analyzing the highly oxidized organic products of lower volatility (e.g. HOM). The

159   CI-APi-TOF is described in more detail in the following section. The aerosol phase measurement was done

160   using (1) a nano-Condensation Nuclei Counter (nCNC), being a combination of a Particle Size Magnifier

161   (PSM, Model A10, Airmodus Ltd.) and a Condensation Particle Counter (CPC, Model A20, Airmodus Ltd.),

162   (2) a Scanning Mobility Particle Sizer (SMPS; Kr-85 neutralizer (Model 3077A, TSI), electrostatic classifier

163 (Model 3082, TSI), nano-water-based CPC (Model 3788, TSI)), counting the size resolved particles from 10

164 nm to 400 nm, (3) a High Resolution Time-Of-Flight Aerosol Mass Spectrometer (HR-TOF-AMS, Aerodyne

165 Research Inc., Jayne et al., 2000) determining the chemical composition of non-refractory aerosol particles

166 larger than ~35 nm. The temperature and relative humidity inside the chamber were monitored using HC02-

167 04 sensors (HygroFlex HF320, Rotronic AG), and the ozone concentration was measured with an ozone

168 monitor (O$_3$-42 Module, Environment S.A.).

169

170 **2.4. Measuring highly oxygenated organic molecules in the gas phase**

171 HOM present in the gas phase were measured using a CI-APi-TOF mass spectrometer. The instrument is

172 described by Jokinen et al. (2012), but also briefly presented here. Strong acids and highly oxygenated organic

173 molecules have been shown to cluster efficiently with nitrate ion (Ehn et al., 2014; Hyttinen et al., 2015).

174 Nitrate ions (i.e. NO$_3^-$, HNO$_3$NO$_3^-$ and (HNO$_3$)$_2$NO$_3^-$), produced by exposure of nitric acid vapors to soft X-

175 ray radiation, were electrostatically introduced into the sample flow of 10 LPM with a reaction time of roughly

176 200 ms at atmospheric pressure. The ions, clusters with NO$_3^-$, were sampled through a 300 µm critical orifice

177 into the APi, where ions were guided and focused by two segmented quadrupoles through chambers with

178 gradually decreasing pressures (~2 mbar and ~10^{-2} mbar, respectively). Finally, an ion lens assembly, at ~10^{-5}

179 mbar, guided the ions into the TOF chamber (~10^{-6} mbar) where they were orthogonally extracted and their

180 mass-to-charge ratios determined. The detected signal of each ion is then expressed as counts per second (cps)

181 or counts per second normalized by the sum of reagent (nitrate) ions (norm. cps). More detail about the APi-

182 TOF itself can be found in Junninen et al. (2010). Quantification of HOM remains challenging, and, in this

183 work, we aim at explaining the relative changes of HOM measured at different temperature rather than

184 focusing on their absolute concentration. However, in some instances, we also estimate absolute quantities by

185 applying a calibration factor C = 1.65 · 10^9 molecules cm^{-3}, (cf. Jokinen et al., 2012, for details on C). As no

186 calibrations were performed during the ACCHA experiments, the value was taken from a sulfuric acid

187 calibration (methodology according to Kürten et al., 2012) performed during an earlier measurement

188 campaign. While associated with a large uncertainty (estimated to be at least -50 % / +100 %), using this value

189 we obtained HOM molar yields (as described in later sections) of a similar range as earlier studies (Jokinen et

190 al., 2012; Ehn et al., 2014).

2.5. HOM dynamics in a batch mode chamber

Being configured in batch mode, without active mixing, the AURA chamber is a dynamic reactor where concentrations of products are a function of cumulative sources and cumulative sinks from the start of the experiment. In the case of HOM, their lifetime in the gas phase must be short due to their low vapor pressure and, thus, their fast condensation. This means that the measured HOM concentrations are mainly the result of production and loss having occurred within the previous minutes, as described in more detail in the following section.

The temporal change in HOM concentrations (i.e. $\frac{d[HOM]}{dt}$) can be expressed as the sum of the production terms and loss terms. The HOM formation is governed by the VOC reaction rate while the loss is dominated by condensation onto particles or walls. For the yield estimation analysis, we focus mainly on the high concentration experiments (i.e. [α-pinene] = 50 ppb), where the high condensation sink (CS, on the order of 0.1 s^{-1}) will dominate over the wall loss rate. In a smaller chamber with active mixing, the wall loss rate for low-volatile species has been estimated to be around 10^{-2} s^{-1} (Ehn et al., 2014), and in the AURA chamber we expect it to be much slower, likely on the order of 10^{-3} s^{-1}. Therefore, we can formulate simplified expression as in the following equations:

$$\frac{d[HOM]}{dt} = \gamma_{HOM} \cdot k \cdot [VOC] \cdot [O_3] - CS \cdot [HOM] \qquad (Eq.\,1)$$

$$\gamma_{HOM} = \frac{\frac{d[HOM]}{dt} + CS \cdot [HOM]}{k \cdot [VOC] \cdot [O_3]} \qquad (Eq.\,2)$$

Herein, γ_{HOM} corresponds to the HOM yield. The temperature-dependent rate constant of α-pinene ozonolysis, k, was taken to be $8.05 \cdot 10^{-16}$ e$^{-640/(273.15+T)}$ cm^3 molecules^{-1} s^{-1}, where T is the temperature in degrees Celsius, (Atkinson, 2000; Calvert et al., 2002). Since the majority of HOM are irreversibly lost upon contact with a surface (Ehn et al., 2014), the CS represents the total sink at a time t. The CS was estimated for an "average HOM", in this case $C_{10}H_{16}O_7$ (being one of the most abundant HOM), using the measured particle number size

217   distributions from the SMPS. The molecular properties that govern the CS are the mass accommodation

218   coefficient, the molecular diffusion coefficient and the mean molecular speed. Based on the work by Julin et

219   al. (2014), the mass accommodation coefficient was set to unity. The molecular diffusion coefficient was

220   calculated using Fuller's method (Tang et al., 2015) and the mean molecular speed was calculated using kinetic

221   theory. Both the molecular diffusion and speed depend on the absolute temperature during the experiments.

222   With the aforementioned assumptions, a distinct yield for each identified HOM of interest can be derived based

223   on Eq. 2, as the slope of a linear fit to the data during an experiment, with $k \cdot [VOC] \cdot [O_3]$ on the x-axis and

224    $\frac{d[HOM]}{dt} + CS \cdot [HOM]$ on the y-axis.

225

3. Results & Discussion

227

3.1. Effect of the temperature on the CI-APi-TOF

229   Since this work targets the variation of HOM in relation to temperature, it is necessary to assess the reliability

230   of the CI-APi-TOF measurement towards temperature variations. The sensitivity towards a certain molecule

231   depends to first approximation on the charging efficiency in the CI inlet and the transmission efficiency of the

232   sampled ion in the APi-TOF. The charging efficiency of a HOM is primarily determined by the stability of the

233    $HOM \cdot NO_3^-$ cluster relative to the $HNO3 \cdot NO_3^-$ cluster (Hyttinen et al., 2015), and we do not expect

234   temperature to cause a large difference in this relative behavior. However, the transmission can be sensitive to

235   small changes, and especially pressures inside the instrument are important to monitor, as the optimal voltages

236   guiding the sampled ions through the instrument have been tuned for specific pressures. The pressures of the

237   two quadrupole chambers (named "SSQ" and "BSQ", respectively, where the pressure dependence is the

238   largest) as well the Total Ion Count (TIC, i.e. sum of all signals), the Reagent Ion Count (RIC, i.e. sum of

239   nitrate ion signals) and the contributions of each nitrate ion signals are presented in Figure 1. The SSQ

240   pressures (Fig. 1a) were found relatively stable (average: ~2.07 mbar) and the BSQ averaged pressure (Fig.

241   1b) was ~$3.3 \cdot 10^{-2}$ mbar, which are typical values for this instrument. Unfortunately, the other instrumental

242   pressures (i.e. ion lens assembly chamber or TOF chamber pressures) were not recorded due to sensor failures.

243   However, as these chambers are at low enough pressures that ion-gas collisions are very rare, any possible

244   small variations in the pressures are unlikely to affect our results. When going from the coldest temperature (-

245   15 °C) to the highest (20 °C), in a continuous temperature ramp, the SSQ pressure decreased by ~0.01 mbar,

246   corresponding to a relative change of 0.5 % (Fig. 1a). Over the same temperature range, the pressure within

247   the second chamber (BSQ) decreased by ~$1.5 \cdot 10^{-3}$ mbar (~4.5 %) when the temperature varied by 35 °C (Fig.

248   1a). The same characteristics were observed when comparing across experiments performed at constant

249   temperatures and for the continuous temperature ramping experiments. The SSQ pressure values below 2.02

250   mbar at -15 °C and 20 °C, corresponding also to the lowest BSQ pressures measured, were related to

251   particularly low ambient pressures (~981.8 mbar). Thus, the effect of temperature within the AURA chamber

252   caused smaller variability of the internal pressures than ambient pressure changes.

253
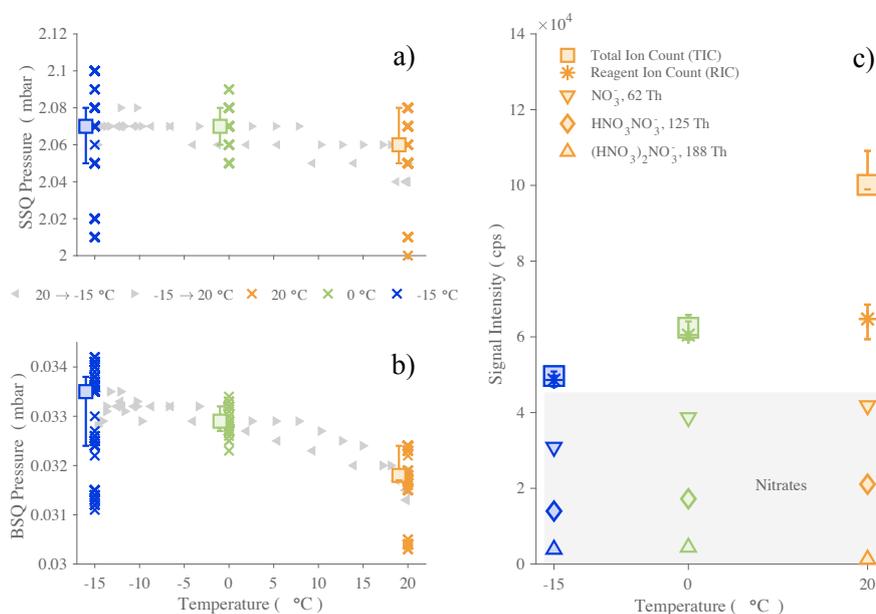
254

255

256   Figure 1: Evolution of the CI-APi-TOF pressures in the first (a) and second (b) quadrupole chambers (SSQ and BSQ, respectively) and

257   signal counts (c) as a function of temperature in the AURA chamber. The APi pressures (panels a & b) are represented by crosses,

258   depicting 10-minute averaged data points for all α-pinene ozonolysis experiments, colored by temperature (blue for -15 °C, green for

259   0 °C and orange for 20 °C). The squares are the median values for each temperature with their 75th and 25th percentiles. Additionally,

260   the gray triangles relate the data (10-minute averages) of two temperature ramp experiments, from -15 °C to 20 °C (right-pointing

261   triangles) or from 20 °C to -15 °C (left-pointing triangles). Panel c) shows averages of the sum of all ion signals (TIC, square-markers)

262   and the sum of all reagent ion signal (RIC, asterisks-markers). RIC markers also include 25th and 75th percentiles. Nitrate signal

263   contributions are also included separately (markers in gray-shaded area: down pointing triangle for NO_3^-, diamond marker for

264    $HNO_3NO_3^-$ and triangle pointing upward for $(HNO_3)_2NO_3^-$).

265

266   The RIC signal (Fig. 1c) stayed within the range $5\text{-}7 \cdot 10^4$ cps, with its lowest values observed at -15 °C. The

267   comparatively larger increase in TIC at the highest temperature is mainly explained by the fact that much

268   higher HOM concentrations were formed at 20 °C compared to lower temperature experiments, and the

269   transmission at these masses is generally higher than in the region of the reagent ions (Junninen et al., 2010;

270   Ehn et al., 2011; Heinritzi et al., 2016). We conclude from the above investigations that changes on the order

271   of tens of percent occurred in our instrument as the AURA chamber temperature was varied, and that only

272   signal changes larger than this should be attributed to actual perturbations in the chemistry taking place in the

273   chamber.

274

275   **3.2. Ozonolysis reaction in the AURA chamber: a typical α-pinene experiment at 20 °C**

276   Selected gas phase precursors and products, including aerosols, for a high-load (i.e. 50 ppb, during 12-Jan-

277   2017) α-pinene oxidation experiment at 20 °C are shown in Figure 2. The steep increase in α-pinene

278   concentration, measured by PTR-TOF-MS, indicates the start (defined as time 0) of the oxidation reaction

279   experiment (Fig. 2a). The formed aerosol product, i.e. particle number and aerosol mass, are presented in Fig.

280   2c. Herein, we observe an increase of the aerosol mass over the first two hours of the experiment whereas the

281   particle number concentration plateaued in the first ten minutes after VOC injection. On the other hand, the

282   HOM signals (Fig. 2b) show a large increase immediately as the VOC was injected. A smaller increase was

283   also observed when the ozone was introduced, most likely due to residual volatiles reacting with ozone inside

284   the chamber. After the first 10 min, HOM signals start to decrease as the CS (Fig. 2d) rapidly increases under

285   these high aerosol loads. After the first half hour, the CS only changes by some tens of percent, while the

286   VOC oxidation rate (gray crosses in Fig. 2b) decreases around one order of magnitude over the following

287   hours of the experiment. Therefore, concentrations of low-volatile HOM should largely track the decay rate of

288   the VOC oxidation rate, which is also observed. We observe a slower decay of HOM monomers than dimers,

289   suggesting that some of the monomers may be semi-volatile enough to not condense irreversibly upon every

290   collision with a surface, and/or that the VOC oxidation rate also influences the formation chemistry, as

291   discussed in more detail in later sections.

292
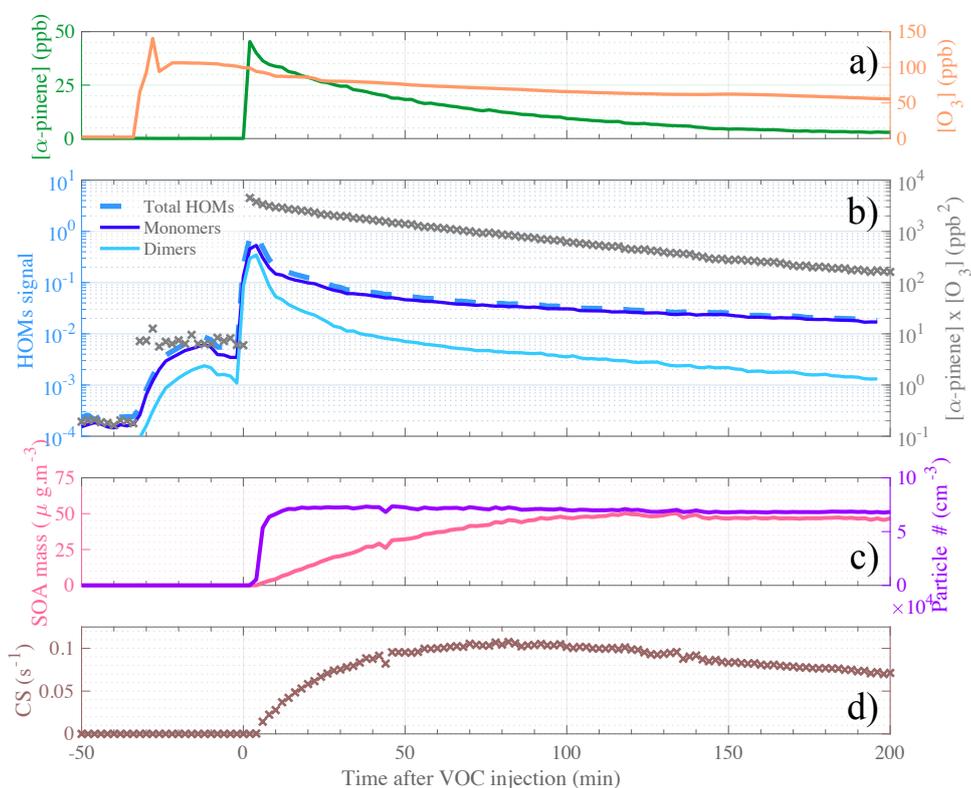
293

294   **Figure 2:** Temporal evolution of the main parameters during a typical α-pinene ozonolysis experiment (initial conditions: [α-pinene]

295   = 50 ppb, [O₃] = 100 ppb, T = 20 °C). Reactant concentrations are shown in Panel a, with α-pinene concentration in dark green and

296   ozone concentration in orange. HOM signals are plotted in Panel b, with a distinction between Total HOM (dashed medium-blue line),

297   HOM monomers ($C_{10}H_{14-16}O_{7-11}$, dark blue line) and HOM dimers ($C_{19-20}H_{28-32}O_{10-18}$ light blue line), as well as the product [α-pinene]

298   · [O₃] represented by gray cross markers. Panel c depicts the SOA mass (pink line) and the particle concentration (purple line). Panel

299   d shows the evolution of the condensation sink. The time span (in x-axis) is expressed as minutes after α-pinene injection, thus the

300   time zero represents the start of the experiment.

301

302   For a more detailed investigation at the HOM formation upon the reaction between ozone and α-pinene, we

303   compare compounds observed in the range between 300 – 600 Thomson (Th) in the CI-APi-TOF, during a

304   background measurement before and 10 min after α-pinene injection for each temperature (Figure 3). The

305   largest HOM signals, highlighted in darker colors, are primarily observed at the highest temperature, but also

306   in the monomer area (300 – 375 Th). The dimer signals (between 450 – 600 Th) are smaller, but still contribute

307   significantly to the total HOM concentration. With the exception of the -15 °C experiment where HOM dimers

308   already reach the background level after 10 min, all molecules selected as representative HOM are present in

309   all the spectra. The detailed peak list of HOM compounds, selected for their high signal intensity, including

310   exact masses and elemental composition is provided in the Appendix (Table A2).

311
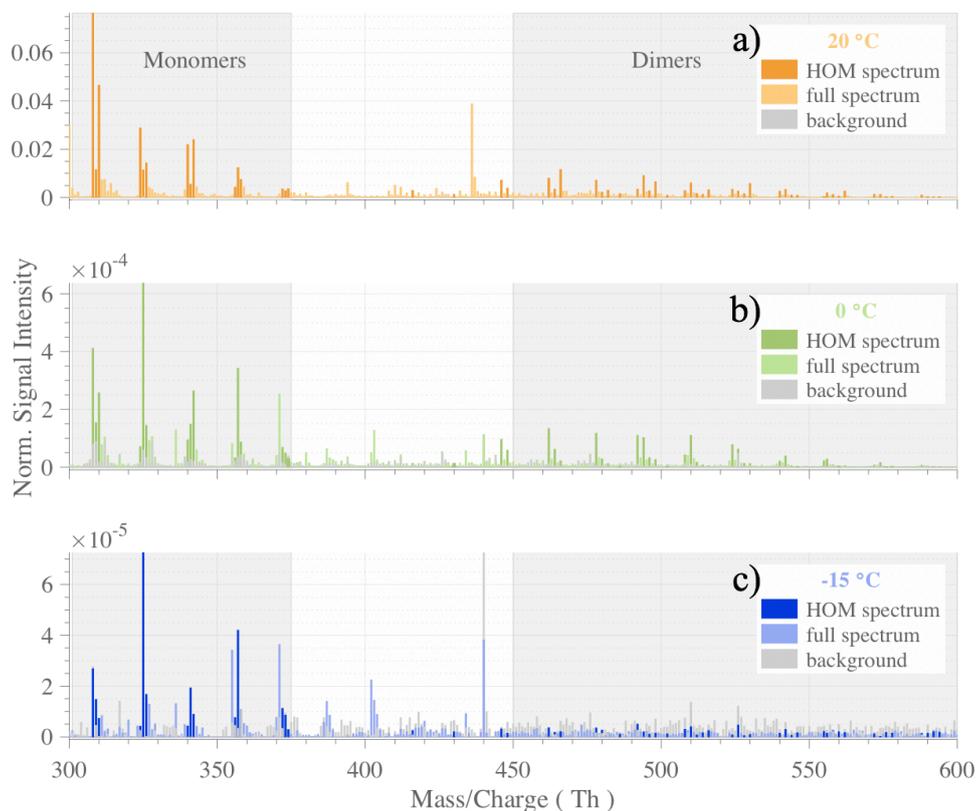
312

313   **Figure 3:** Typical HOM mass spectra observed during α-pinene ozonolysis experiments (initial conditions: [α-pinene] = 50 ppb, [O₃]

314   = 100 ppb,) at T = 20 °C (panel a) in orange, T = 0 °C (panel b) in green, T = -15 °C (panel c) in blue. The normalized signals were

315   averaged over 2 minutes during background measurement before VOC injection (gray bars), and 10 min after α-pinene injection

316   (colored bars). Specific masses, selected for representing high-intensity HOM, are highlighted in darker colors. Gray-shaded areas

317   show HOM sub-ranges of monomers and dimers.

318

319

320   **3.3. Effect of the temperature on measured HOM**

321   We performed a total of twelve α-pinene ozonolysis experiments with seven at high loading (i.e. [α-pinene] =

322   50 ppb), out of which two were conducted at 20 °C, two at 0 °C and three at -15 °C. Three experiments were

323   performed with [α-pinene] = 10 ppb – one for each aforementioned temperature. Experiments with 50 ppb of

324   β-pinene were also performed at the same three temperatures (see Table A2). An overview of HOM

325   measurements for the different experiments is shown in Figure 4, with distinction between HOM monomers

326   (Fig. 4a) and dimers (Fig4. b) as defined earlier.

327
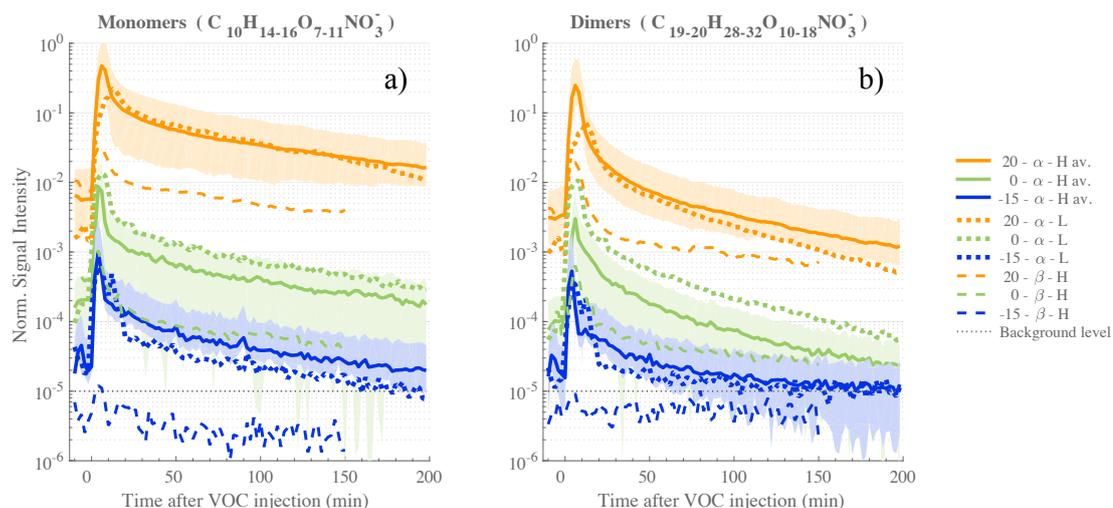
328

329   **Figure 4:** Time series of HOM measured during the ACCHA campaign. HOM monomer (a) and dimer (b) traces include compounds

330   with a chemical composition of $C_{10}H_{14-16}O_{7-11}$ and $C_{19-20}H_{28-32}O_{10-18}$, respectively. The series are colored based on temperature, orange

331   for 20 °C experiments, green for 0 °C and blue for -15 °C. Statistics over α-pinene ("α" in the legend) high load (50 ppb, "H")

332   experiments are shown, with averaged values ("av." in continuous line) and the maximum and minimum values of the measured HOM

333   signal (bounded shaded area). α-pinene low load (L) experiments are symbolized with colored dotted lines and the β-pinene ("β")

334   experiments by dashed lines. The gray dotted line depicts the estimated background level of the CI-APi-TOF.

335

336   For a similar experiment type (i.e. same initial VOC concentrations), it can be seen that the resulting HOM

337   concentrations were considerably impacted by the temperature at which the oxidation reaction occurred. The

338   signal intensity for HOM monomers from α-pinene measured 30 minutes after the VOC injection was roughly

339   two orders of magnitudes higher at 20 °C compared to 0 °C, and about three orders of magnitude higher

340   compared to the -15 °C experiment. Very similar behavior is observed with respect to temperature for the

341   dimer species as well, but with the differences that (1) less dimers are found in comparison to the HOM

342   monomers and (2) HOM dimer concentrations are found to decrease at a faster rate during the experiment. The

343   faster decrease of dimers compared to monomers results either from a lower production or a higher loss for

344   dimers towards the end of the experiments. We expect that the reduced [α-pinene] and [O_3], leading to slower

345   oxidation rates and consequently lower [RO_2] will have a greater impact on the dimers than the monomers, as

346   the formation rate of dimers is proportional to [RO_2]^2, while monomers can still be formed efficiently via other

347   RO_2 termination pathways, as discussed earlier.

348

349   When comparing the high (50 ppb) and low (10 ppb) loading α-pinene experiments, HOM signals were within

350   the same range of concentration, and even higher at 0 °C the HOM were even more abundant in the low initial

351   VOC concentration. Although this result may seem surprising at first, it only verifies our assumptions in Eq.

352   1 that the HOM concentration is a relatively simple function of formation and loss rates. Despite the fact that

353   the low-concentration experiments had five times lower [VOC] (and consequently five times lower HOM

354   formation rate), the condensation sink, being the primary loss for HOM, was ~8 times due to reduced aerosol

355   formation. In other words, the loss rates decreased more than the formation rate when the precursor

356   concentration was lowered, resulting in an increase of [HOM].

357

358   Finally, the use of β-pinene as HOM precursor produced significantly less HOM, with concentrations being

359   more than a factor of 10 lower compared to experiments performed with α-pinene at the same conditions. This

360 agrees with earlier studies (Jokinen et al., 2014; Ehn et al., 2014) which have shown clearly lower HOM yields

361 for β-pinene compared to α-pinene ozonolysis. The difference is primarily attributed to the exocyclic double

362 bond in β-pinene. Note that, the β-pinene HOM concentrations at the lowest temperature, -15 °C, were below

363 the instrumental limit of detection.

364

365 **3.4. Yield estimation and temperature influence for molecule-specific HOM**
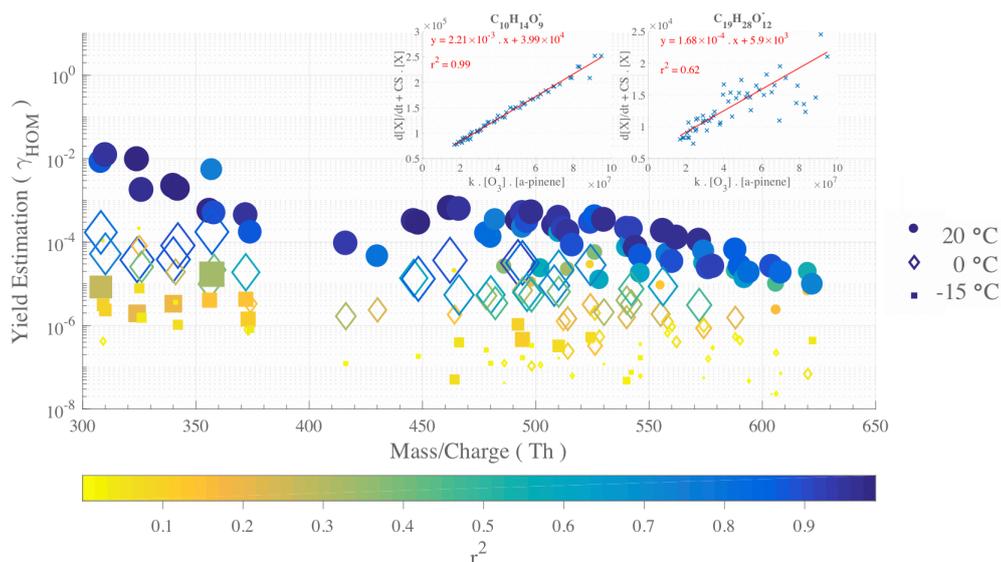
366

367 **Figure 5:** Yield estimations for individual α-pinene HOM from linear fits at 20 °C, 0 °C and -15 °C. Filled circles symbolize data from

368 a 20 °C experiment (12-Jan-2017), diamond symbols illustrate 0 °C data (16-Jan-2017), and the filled squares represents -15 °C data

369 (13-Jan-2017). The markers are colored and sized by r^2 values, coefficient of determination, evaluating the goodness of the linear fit

370 used to derive the yields. The top-right insets show two examples (for $C_{10}H_{14}O_9$ and $C_{19}H_{28}O_{12}$) of the yield determination by robust

371 linear fits to the variables described in the methods section.

372

373 We determined yield estimates, individually for each HOM of interest, from the results of a robust linear fit as

374 described in the methods section and Eq. 2. The yield results are shown in Figure 5, with fit examples shown

375 for $C_{10}H_{14}O_9$ and $C_{19}H_{28}O_{12}$ in the insets. As expected, based on Figure 4, the retrieved yield values (γ_{HOM})

376   decrease considerably with colder reaction conditions, with a total HOM yield (i.e. sum of the individual yields

377   for each temperature) found to be 5.2 % at 20 °C, 0.10 % at 0 °C and $6.3 \cdot 10^{-3}$ % at -15 °C.

378   We again emphasize the large uncertainties in these absolute estimates, but the HOM yield estimated for T =

379   20 °C does agree well with earlier reported values (e.g. Ehn et al. (2014), Jokinen et al. (2014), Sarnela et al.

380   (2018)). As the largest contribution to the HOM yield comes from the least oxidized monomers (e.g. high

381   signal intensity at 308 Th and 310 Th for $C_{10}H_{14}O_7$ and $C_{10}H_{16}O_7$ respectively), the molar yield may be slightly

382   over-estimated, especially at 20 °C, due to the loss rates possibly being lower than assumed if these HOM are

383   not condensing irreversibly onto the aerosol. γ_{HOM} values are on average higher for HOM monomers than for

384   dimers, with the overall shape of the distribution closely resembling the mass spectrum in Figure 3. We

385   performed the same calculation for the experiment were [α-pinene] = 10 ppb and found total HOM-yields in

386   the same range, as the numbers found at 50 ppb, considering our estimated uncertainty: 8.8 % at 20 °C, 0.25

387   % at 0 °C and $5.5 \cdot 10^{-3}$ % at -15 °C. The slightly higher values may indicate that at the higher loadings,

388   bimolecular RO2 termination reactions are already occurring so fast that autoxidation is hampered. The total

389   HOM yield decrease when going from 20 °C to 0 °C decreased by a factor 50 at the higher loadings, while the

390   corresponding value at lower loadings was 35.

391
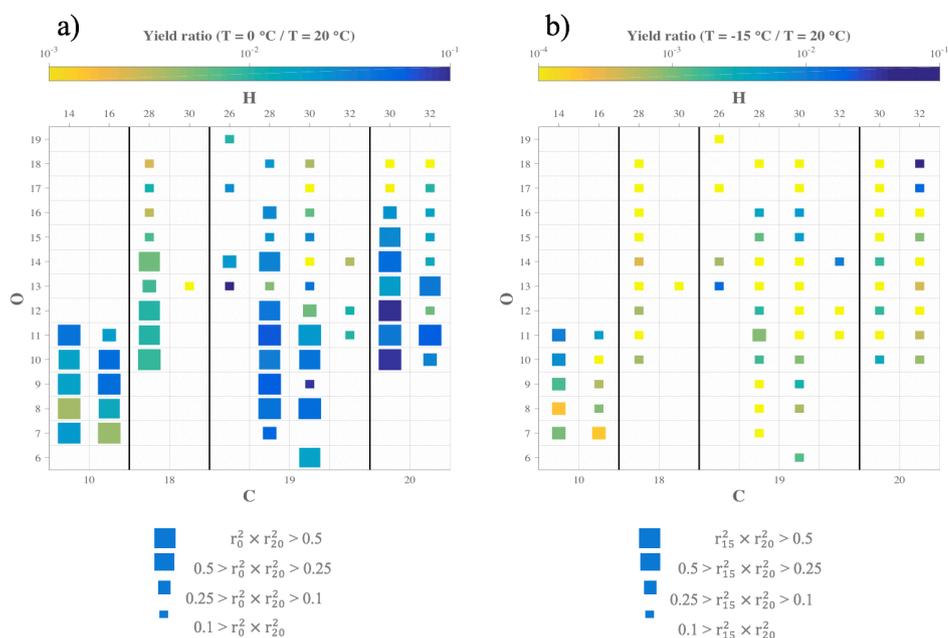
392   **Figure 6:** Comparison of yields for specific HOM compositions at different temperatures. Each square symbolizes a specific HOM

393   measured by the CI-APi-TOF. The elemental composition can be read by taking the number of C atoms from the bottom axis, the

394   number of H atoms from the top axis, and the number of O atoms from the left axis. The size of the square depicts the goodness of fit

395   (r^2) used to derive the yields, and color shows the ratio of the yield at 0 °C (Panel a) or -15 °C (Panel b) compared to the yield measured

396   at 20 °C.

397

398   While Figure 5 showed the estimated yields for every HOM at every temperature probed, specific chemical

399   composition cannot be read from the plot. In order to assess the impact of temperature of the yield of HOM

400   based on each elemental composition, Figure 6 depicts for each compound the ratio of the yield at 0 °C (Fig.

401   6a) or -15 °C (Fig. 6b) compared to the yield at 20 °C for a high load experiment of α-pinene ozonolysis. In

402   Fig. 6a, many larger squares are observable, indicating a good reliability of our comparison analysis, but in

403   Fig. 6b, it is clear that the HOM concentrations at the lowest temperature were too low to provide much reliable

404   compound-specific information. From Fig. 6a we see no clear trend in the yield change for any column (i.e.

405   changing oxygen content HOM with a given amount of C and H). The HOM yields yield ratios between the

406   two temperatures are primarily within 10^{-2} – 10^{-1}, meaning that the molecule-specific yields dropped to

407   between 1-10% when temperature decreased from 20 °C to 0 °C. If autoxidation of RO2 decreased this

408   considerably, one could have expected the more oxygenated HOM to decrease more than the less oxygenated

409   ones. However, this did not seem to be the case, as e.g. some of the most abundant HOM $C_{10}H_{14}O_7$, $C_{10}H_{14}O_9$,

410   and $C_{10}H_{14}O_{11}$ seemingly decreased the same amounts. One possible interpretation of this is that the rate-

411   limiting step in the autoxidation chain takes place in RO_2 radicals with 6 or less O atoms, which are not detected

412   with our CI-APi-TOF, while the later H-shift reactions are fast enough that other reactions still do not become

413   competitive. These "non-HOM" RO_2 radicals may then also be key molecules for determining the final

414   branching leading to the different observed HOM with 7 or more O atoms. This may shed light on one of the

415   main open challenges (Ehn et al., 2017) in understanding HOM formation, namely how RO_2 radicals with e.g.

416   6, 8 and 10 O atoms can form within a second, yet the relative distribution of these three does not change if

417   the reaction time is allowed to increase (Berndt et al., 2015). Since the O_{10}-RO_2 (or its closed shell products)

418   are not seen to accumulate over time, our results here provide support for a pathway where the O_6- and O_8-

419   RO_2 are to some extent "terminal" products incapable of further fast H-shift reactions, while the O_{10}-RO_2 has

420   been formed via another branch of the reaction where the autoxidation is able to proceed further. In this branch,

421   the O_6- and O_8-RO_2 are likely only short-lived intermediates. While in no way conclusive, this highlights the

422   need for fast measurements of HOM formation as well as improved techniques for observing less oxidized

423   RO_2 radicals.

424

425   The only compound group where a slight decrease can be seen as a function of O-atom content is the

426   C20H30On dimers. Interestingly, these also show some of the smallest yield ratios of all compounds. At the

427   same time, the level of C_{18} dimers appears to drop most of all compound groups, potentially suggesting that

428   the mechanism through which carbon atoms were lost on the way to the C_{18} dimers was sensitive to

429   temperature, and at 0 °C the fragmentation was less prominent. It is conceivable that the different branching

430   at 0 °C caused some of the C18 dimer precursors to form C20 dimers instead. However, this issue would need

431   more detailed experiments in order to verify.

432

433   The decrease in HOM yield due to slower RO_2 H-shift rates at lower temperatures was found to be very

434   dramatic under our conditions. However, the exact magnitude of this decrease in HOM yield is determined by

435   the processes competing with the H-shifts. Under our conditions, the RO_2 lifetime is kept quite short, both due

436   to bimolecular ($RO_2 + RO_2$ or $RO_2 + HO_2$) reactions and collisions with particles, and therefore any reduction

437   in H-shift rates can strongly reduce the HOM yield. Inversely, under very low loadings, the RO_2 lifetime may

438   be long enough that the temperature decreases from 20 °C to 0 °C may cause much smaller changes in the

439   HOM yields. If the lifetime of RO_2 radicals is clearly longer than the time needed for multiple consecutive H-

440   shifts to take place, HOM yields would decrease only marginally with temperature. In the atmosphere, RO2

441   lifetime will often be governed by NO, which means that there can exist an intricate dependence of HOM

442   yields as a function of temperature, VOC type, VOC oxidation rate, and NO_X.

443

4. Conclusion

445

446 We present laboratory studies of HOM formation from monoterpene ozonolysis at different temperatures (20

447 °C, 0 °C, and -15 °C). Our main insight is that temperature considerably impacted the HOM formation,

448 decreasing the observed HOM yield by around 50-fold upon a decrease by 20 °C. The exact temperature

449 dependence of HOM formation in general is likely both VOC- and loading-dependent, due to the competition

450 between autoxidation and termination reactions, and will likely be smaller at lower loadings. While

451 autoxidation is expected to decrease with temperature, our result is still striking as it takes place over a

452 temperature range which is atmospherically relevant for areas where monoterpene emissions are abundant, e.g.

453 the boreal forest. One important observation was that HOM were present at all measured temperatures with

454 roughly similar spectral distributions. This suggested that the total HOM yield as well as the final HOM

455 distribution are mainly determined by the first H-shift steps, i.e. in the region where the CI-APi-TOF is unable

456 to measure. This highlights the need for more comprehensive observations of autoxidation, allowing direct

457 observations of the critical steps determining the HOM yields and, subsequently, the production rate of low-

458 volatile organic compounds able to form secondary organic aerosol.

459

460 **Authors Contribution**

461

462 M. Ehn, M. Bilde, and M. Glausius supervised the ACCHA campaign. L.L.J Quéléver, K. Kristensen, M. Bilde

463 and M. Ehn designed the experiments. K. Kristensen and L. N. Jensen initialized the chamber for experiments.

464 L.L.J. Quéléver performed the measurement and analyzed the gas-phase HOM. K. Kristensen and L. N. Jensen

465 measured and analyzed the aerosol phase. K. Kristensen, B. Rosati and R. Teiwes measured and analyzed the

466 VOCs and their semi-volatile oxidation production. M. Ehn, K. Daellenbach, O. Peräkylä and P. Roldin guided

467 and helped the analysis of HOM yield performed by L.L.J. Quéléver. L. L. J. Quéléver prepared the manuscript

468 with the contribution from all co-authors.

469

470 **Acknowledgments**

471

498   Calvert, J. G., Atkinson, R., Becker, K. H., Kamens, R. M., Seinfeld, J. H., Wallington, T. H., and Yarwood,

499   G.: The mechanisms of atmospheric oxidation of the aromatic hydrocarbons, Oxford University Press, 2002.

500   Crounse, J. D., Nielsen, L. B., Jørgensen, S., Kjaergaard, H. G., and Wennberg, P. O.: Autoxidation of organic

501   compounds in the atmosphere, The Journal of Physical Chemistry Letters, 4, 3513-3520, 2013.

502

503   Donahue, N. M., Kroll, J., Pandis, S. N., and Robinson, A. L.: A two-dimensional volatility basis set–Part 2:

504   Diagnostics of organic-aerosol evolution, Atmospheric Chemistry and Physics, 12, 615-634, 2012.

505

506   Donahue, N. M., Ortega, I. K., Chuang, W., Riipinen, I., Riccobono, F., Schobesberger, S., Dommen, J.,

507   Baltensperger, U., Kulmala, M., and Worsnop, D. R.: How do organic vapors contribute to new-particle

508   formation?, Faraday discussions, 165, 91-104, 2013.

509

510   Dusek, U., Frank, G., Hildebrandt, L., Curtius, J., Schneider, J., Walter, S., Chand, D., Drewnick, F., Hings,

511   S., and Jung, D.: Size matters more than chemistry for cloud-nucleating ability of aerosol particles, Science,

512   312, 1375-1378, 2006.

513

514   Ehn, M., Junninen, H., Petäjä, T., Kurtén, T., Kerminen, V.-M., Schobesberger, S., Manninen, H., Ortega, I.,

515   Vehkamäki, H., and Kulmala, M.: Composition and temporal behavior of ambient ions in the boreal forest,

516   Atmospheric Chemistry and Physics, 10, 8513-8530, 2010.

517

518   Ehn, M., Junninen, H., Schobesberger, S., Manninen, H. E., Franchin, A., Sipilä, M., Petäjä, T., Kerminen, V.-

519   M., Tammet, H., and Mirme, A.: An instrumental comparison of mobility and mass measurements of

520   atmospheric small ions, Aerosol Science and Technology, 45, 522-532, 2011.

521

522   Ehn, M., Kleist, E., Junninen, H., Petäjä, T., Lönn, G., Schobesberger, S., Maso, M. D., Trimborn, A., Kulmala,

523   M., and Worsnop, D.: Gas phase formation of extremely oxidized pinene reaction products in chamber and

524   ambient air, Atmospheric chemistry and physics, 12, 5113-5127, 2012.

525

526   Ehn, M., Thornton, J. A., Kleist, E., Sipilä, M., Junninen, H., Pullinen, I., Springer, M., Rubach, F., Tillmann,

527   R., and Lee, B.: A large source of low-volatility secondary organic aerosol, Nature, 506, 476, 2014.

528

529   Ehn, M., Berndt, T., Wildt, J., and Mentel, T.: Highly Oxygenated Molecules from Atmospheric Autoxidation

530   of Hydrocarbons: A Prominent Challenge for Chemical Kinetics Studies, International Journal of Chemical

531   Kinetics, 49, 821-831, 2017.

532

533   Frege, C., Ortega, I. K., Rissanen, M. P., Praplan, A. P., Steiner, G., Heinritzi, M., Ahonen, L., Amorim, A.,

534   Bernhammer, A.-K., and Bianchi, F.: Influence of temperature on the molecular composition of ions and

535   charged clusters during pure biogenic nucleation, Atmospheric Chemistry and Physics, 18, 65-79, 2018.

536

537   Hallquist, M., Wenger, J. C., Baltensperger, U., Rudich, Y., Simpson, D., Claeys, M., Dommen, J., Donahue,

538   N., George, C., and Goldstein, A.: The formation, properties and impact of secondary organic aerosol: current

539   and emerging issues, Atmospheric chemistry and physics, 9, 5155-5236, 2009.

540

541   Heinritzi, M., Hansel, A., Simon, M., Steiner, G., Wagner, A. C., Kürten, A., and Curtius, J.: submitter:

542   Characterization of the mass-dependent transmission efficiency of a CIMS, Atmos. Meas. Tech., 9, 1449-

543   1460, 2016.

544

545   Hyttinen, N., Kupiainen-Määttä, O., Rissanen, M. P., Muuronen, M., Ehn, M., and Kurtén, T.: Modeling the

546   charging of highly oxidized cyclohexene ozonolysis products using nitrate-based chemical ionization, The

547   Journal of Physical Chemistry A, 119, 6339-6345, 2015.

548

549   IPCC: Climate change 2013: the physical science basis. Contribution of the Working Group 1 to the Fifth

550   Assessment Report (AR5) of the Intergovernmental Panel on Climate Change, edited by: Stocker, T. F., Qin,

551   D., Plattner, G., Tignor, M., Allen, S., Boschung, J., Nauels, A., Xia, Y., Bex, V., and Midgley, P. M.,

552   Cambridge University Press, Cambridge (UK), New York (USA), 2013.

553

554   Jayne, J. T., Leard, D. C., Zhang, X., Davidovits, P., Smith, K. A., Kolb, C. E., and Worsnop, D. R.:

555   Development of an aerosol mass spectrometer for size and composition analysis of submicron particles,

556   Aerosol Science & Technology, 33, 49-70, 2000.

557

558   Jenkin, M. E., Saunders, S. M., and Pilling, M. J.: The tropospheric degradation of volatile organic compounds:

559   a protocol for mechanism development. Atmospheric Environment 31, 81–104, 1997.

560

561   Jenkin, M. E., Young, J. C., and Rickard, A. R.: The MCM v3.3.1 degradation scheme for isoprene. Atmos.

562   Chem. Phys. 15, 11433–11459, 2015.

563

564   Jimenez, J. L., Canagaratna, M. R., Donahue, N. M., Prevot, A. S., Zhang, Q., Kroll, J. H., DeCarlo, P. F.,

565   Allan, J. D., Coe, H., Ng, N. L., Aiken, A. C., Docherty, K. S., Ulbrich, I. M., Grieshop, A. P., Robinson, A.

566   L., Duplissy, J., Smith, J. D., Wilson, K. R., Lanz, V. A., Hueglin, C., Sun, Y. L., Tian, J., Laaksonen, A.,

567   Raatikainen, T., Rautiainen, J., Vaattovaara, P., Ehn, M., Kulmala, M., Tomlinson, J. M., Collins, D. R.,

568   Cubison, M. J., Dunlea, E. J., Huffman, J. A., Onasch, T. B., Alfarra, M. R., Williams, P. I., Bower, K., Kondo,

569   Y., Schneider, J., Drewnick, F., Borrmann, S., Weimer, S., Demerjian, K., Salcedo, D., Cottrell, L., Griffin,

570   R., Takami, A., Miyoshi, T., Hatakeyama, S., Shimono, A., Sun, J. Y., Zhang, Y. M., Dzepina, K., Kimmel, J.

571   R., Sueper, D., Jayne, J. T., Herndon, S. C., Trimborn, A. M., Williams, L. R., Wood, E. C., Middlebrook, A.

572   M., Kolb, C. E., Baltensperger, U., and Worsnop, D. R.: Evolution of organic aerosols in the atmosphere,

573   Science, 326, 2009.

574

575   Jokinen, T., Sipilä, M., Junninen, H., Ehn, M., Lönn, G., Hakala, J., Petäjä, T., Mauldin Iii, R., Kulmala, M.,

576   and Worsnop, D.: Atmospheric sulphuric acid and neutral cluster measurements using CI-APi-TOF,

577   Atmospheric Chemistry and Physics, 12, 4117-4125, 2012.

578

579   Jokinen, T., Sipilä, M., Richters, S., Kerminen, V. M., Paasonen, P., Stratmann, F., Worsnop, D., Kulmala,

580   M., Ehn, M., and Herrmann, H.: Rapid autoxidation forms highly oxidized RO_2 radicals in the atmosphere,

581   Angewandte Chemie International Edition, 53, 14596-14600, 2014.

582

583 Jokinen, T., Berndt, T., Makkonen, R., Kerminen, V.-M., Junninen, H., Paasonen, P., Stratmann, F., Herrmann,

584 H., Guenther, A. B., and Worsnop, D. R.: Production of extremely low volatile organic compounds from

585 biogenic emissions: Measured yields and atmospheric implications, Proceedings of the National Academy of

586 Sciences, 201423977, 2015.

587

588 Jordan, A., Haidacher, S., Hanel, G., Hartungen, E., Märk, L., Seehauser, H., Schottkowsky, R., Sulzer, P.,

589 and Märk, T.: A high resolution and high sensitivity proton-transfer-reaction time-of-flight mass spectrometer

590 (PTR-TOF-MS), International Journal of Mass Spectrometry, 286, 122-128, 2009.

591

592 Julin, J., Winkler, P. M., Donahue, N. M., Wagner P. E., and Riipinen, I.: Near-unity mass accommodation

593 coefficient of organic molecules of varying structure. Environ. Sci. Technol., 48(20), 12083-12089, 2014.

594

595 Junninen, H., Ehn, M., Petäjä, T., Luosujärvi, L., Kotiaho, T., Kostiainen, R., Rohner, U., Gonin, M., Fuhrer,

596 K., and Kulmala, M.: A high-resolution mass spectrometer to measure atmospheric ion composition,

597 Atmospheric Measurement Techniques, 3, 1039-1053, 2010.

598

599 Kristensen, K., Jensen, L., Glasius, M., and Bilde, M.: The effect of sub-zero temperature on the formation

600 and composition of secondary organic aerosol from ozonolysis of alpha-pinene, Environmental Science:

601 Processes & Impacts, 19, 1220-1234, 2017.

602

603 Kulmala, M., Kontkanen, J., Junninen, H., Lehtipalo, K., Manninen, H. E., Nieminen, T., Petäjä, T., Sipilä,

604 M., Schobesberger, S., and Rantala, P.: Direct observations of atmospheric aerosol nucleation, Science, 339,

605 943-946, 2013.

606

607 Kürten, A., Rondo, L., Ehrhart, S., and Curtius, J.: Calibration of a chemical ionization mass spectrometer for

608 the measurement of gaseous sulfuric acid, The Journal of Physical Chemistry A, 116, 6375-6386, 2012.

609

610   Mentel, T. F., Springer, M., Ehn, M., Kleist, E., Pullinen, I., Kurtén, T., Rissanen, M., Wahner, A., and Wildt,

611   J.: Formation of highly oxidized multifunctional compounds: autoxidation of peroxy radicals formed in the

612   ozonolysis of alkenes – deduced from structure–product relationships, Atmos. Chem. Phys., 15, 6745-6765,

613

614   Otkjær, R. V., Jakobsen, H. H., Tram, C. M., and Kjaergaard, H. G.: Calculated Hydrogen Shift Rate Constants

615   in Substituted Alkyl Peroxy Radicals, The Journal of Physical Chemistry A, 122, 8665-8673, 2018.

616

617   Praske, E., Otkjær, R. V., Crounse, J. D., Hethcox, J. C., Stoltz, B. M., Kjaergaard, H. G., and Wennberg, P.

618   O.: Atmospheric autoxidation is increasingly important in urban and suburban North America, Proceedings of

619   the National Academy of Sciences, 115, 64-69, 2018.

620

621   Rissanen, M. P., Kurtén, T., Sipilä, M., Thornton, J. A., Kangasluoma, J., Sarnela, N., Junninen, H., Jørgensen,

622   S., Schallhart, S., and Kajos, M. K.: The formation of highly oxidized multifunctional products in the

623   ozonolysis of cyclohexene, Journal of the American Chemical Society, 136, 15596-15606, 2014.

624

625   Rissanen, M. P., Kurtén, T., Sipilä, M., Thornton, J. A., Kausiala, O., Garmash, O., Kjaergaard, H. G., Petäjä,

626   T., Worsnop, D. R., and Ehn, M.: Effects of chemical complexity on the autoxidation mechanisms of

627   endocyclic alkene ozonolysis products: From methylcyclohexenes toward understanding α-pinene, The

628   Journal of Physical Chemistry A, 119, 4633-4650, 2015.

629

630   Sarnela, N., Jokinen, T., Duplissy, J., Yan, C., Nieminen, T., Ehn, M., Schobesberger, S., Heinritzi, M.,

631   Ehrhart, S., and Lehtipalo, K.: Measurement–model comparison of stabilized Criegee intermediate and highly

632   oxygenated molecule production in the CLOUD chamber, Atmospheric Chemistry and Physics, 18, 2363-

633   2380, 2018.

634

635   Saunders, S. M., Jenkin, M. E., Derwent, R. G., and Pilling, M. J.: Protocol for the development of the master

636   chemical mechanism, MCM v3 (part a): tropospheric degradation of non-aromatic volatile organic

637   compounds. Atmos. Chem. Phys., 3, 161–180, 2003.

638

639   Stolzenburg, D., Fischer, L., Vogel, A. L., Heinritzi, M., Schervish, M., Simon, M., Wagner, A. C., Dada, L.,

640   Ahonen, L. R., and Amorim, A.: Rapid growth of organic aerosol nanoparticles over a wide tropospheric

641   temperature range, Proceedings of the National Academy of Sciences, 115, 9122-9127, 2018.

642

643   Tang, M. J., Shiraiwa, M., Pöschl, U., Cox, R. A., and Kalberer, M.: Compilation and evaluation of gas phase

644   diffusion coefficients of reactive trace gases in the atmosphere: Volume 2. Diffusivities of organic compounds,

645   pressure-normalised mean free paths, and average Knudsen numbers for gas uptake calculations. Atmos.

646   Chem. Phys., 15, 5585–5598, 2015.

647

648   Tröstl, J., Chuang, W. K., Gordon, H., Heinritzi, M., Yan, C., Molteni, U., Ahlm, L., Frege, C., Bianchi, F.,

649   and Wagner, R.: The role of low-volatility organic compounds in initial particle growth in the atmosphere,

650   Nature, 533, 527, 2016.

651

652   Zhang, Q., Jimenez, J. L., Canagaratna, M., Allan, J., Coe, H., Ulbrich, I., Alfarra, M., Takami, A.,

653   Middlebrook, A., and Sun, Y.: Ubiquity and dominance of oxygenated species in organic aerosols in

654   anthropogenically-influenced Northern Hemisphere midlatitudes, Geophysical Research Letters, 34, 2007.

655

656   Zhao, J., Ortega, J., Chen, M., McMurry, P., and Smith, J.: Dependence of particle nucleation and growth on

657   high molecular weight gas phase products during ozonolysis of α-pinene, Atmospheric Chemistry and Physics,

658   13, 9319-9354, 2013.

659 **Appendix**

660

661 Table A1 : ACCHA Experiment overview

VOC Concentration (ppb)	[VOC] reacted with O3 * (ppb)	[VOC] reacted with OH * (ppb)	Temperature (℃)	Date
VOC : α- pinene				
50			20	12-Dec-16
50			-15	13-Dec-16
50			0	19-Dec-16
50			-15	21-Dec-16
50	30.1	15.5	20	12-Jan-17
50			-15	13-Jan-17
50	30.0	16.1	0	16-Jan-17
10	6.48	3.04	20	02-Dec-16
10			-15	07-Dec-16
10	6.30	3.14	0	08-Dec-16
10			20 → -15	09-Dec-16
10			-15 → 20	20-Dec-16
VOC : β-pinene				
50			20	03-Jan-17
50			-15	04-Jan-17
50			0	05-Jan-17

* Estimation based on model simulations using the Master Chemical Mechanism v3.3.2 (Jenkin et al.,1997 & 2015; Saunders et al., 2003)

662

663

664     Table A2: Main monoterpene ozonolysis HOM products: Peak list

Monomers		Dimers					
m/z (Th)	Composition*	m/z (Th)	Composition*	m/z (Th)	Composition*	m/z (Th)	Composition*
308.06	$C_{10}H_{14}O_7$	446.17	$C_{19}H_{28}O_8$	514.14	$C_{18}H_{28}O_{13}$	562.13	$C_{18}H_{28}O_{16}$
309.07	$C_{10}H_{15}O_7$	448.18	$C_{19}H_{30}O_8$	514.18	$C_{19}H_{32}O_{12}$	572.15	$C_{20}H_{30}O_{15}$
310.08	$C_{10}H_{16}O_7$	462.16	$C_{19}H_{28}O_9$	516.16	$C_{18}H_{30}O_{13}$	574.13	$C_{19}H_{28}O_{16}$
324.06	$C_{10}H_{14}O_8$	464.18	$C_{19}H_{30}O_9$	524.13	$C_{18}H_{26}O_{13}$	574.16	$C_{20}H_{32}O_{15}$
325.07	$C_{10}H_{15}O_8$	466.16	$C_{18}H_{28}O_{10}$	524.16	$C_{20}H_{30}O_{12}$	576.14	$C_{19}H_{30}O_{16}$
326.07	$C_{10}H_{16}O_8$	478.16	$C_{19}H_{28}O_{10}$	526.14	$C_{19}H_{28}O_{13}$	578.12	$C_{18}H_{28}O_{17}$
340.05	$C_{10}H_{14}O_9$	480.17	$C_{19}H_{30}O_{10}$	526.18	$C_{20}H_{32}O_{12}$	588.11	$C_{19}H_{26}O_{17}$
341.06	$C_{10}H_{15}O_9$	482.15	$C_{18}H_{28}O_{11}$	528.16	$C_{19}H_{30}O_{13}$	588.14	$C_{20}H_{30}O_{16}$
342.07	$C_{10}H_{16}O_9$	486.15	$C_{17}H_{28}O_{12}$	530.14	$C_{18}H_{28}O_{14}$	590.16	$C_{20}H_{32}O_{16}$
356.05	$C_{10}H_{14}O_{10}$	492.17	$C_{20}H_{30}O_{10}$	540.12	$C_{19}H_{26}O_{14}$	592.14	$C_{19}H_{30}O_{17}$
357.05	$C_{10}H_{15}O_{10}$	494.15	$C_{19}H_{28}O_{11}$	540.16	$C_{20}H_{30}O_{13}$	594.12	$C_{18}H_{28}O_{18}$
358.06	$C_{10}H_{16}O_{10}$	494.19	$C_{20}H_{32}O_{10}$	542.14	$C_{19}H_{28}O_{14}$	604.14	$C_{20}H_{30}O_{17}$
372.04	$C_{10}H_{14}O_{11}$	496.17	$C_{19}H_{30}O_{11}$	542.17	$C_{20}H_{32}O_{13}$	606.12	$C_{19}H_{28}O_{18}$
373.05	$C_{10}H_{15}O_{11}$	498.15	$C_{18}H_{28}O_{12}$	544.15	$C_{19}H_{30}O_{14}$	606.15	$C_{20}H_{32}O_{17}$
374.06	$C_{10}H_{16}O_{11}$	498.18	$C_{19}H_{32}O_{11}$	546.13	$C_{18}H_{28}O_{15}$	608.13	$C_{19}H_{30}O_{18}$
		502.14	$C_{17}H_{28}O_{13}$	546.17	$C_{19}H_{32}O_{14}$	620.10	$C_{19}H_{26}O_{19}$
		508.17	$C_{20}H_{30}O_{11}$	556.15	$C_{20}H_{30}O_{14}$	620.13	$C_{20}H_{30}O_{18}$
		510.15	$C_{19}H_{28}O_{12}$	558.13	$C_{19}H_{28}O_{15}$	622.15	$C_{20}H_{32}O_{18}$
		510.18	$C_{20}H_{32}O_{11}$	558.17	$C_{20}H_{32}O_{14}$		
		512.16	$C_{19}H_{30}O_{12}$	560.15	$C_{19}H_{30}O_{15}$		

* Note that all compounds are detected as cluster with Nitrate Ion (NO_3^-)

665

666

667

668